The Astrophysical Journal, 775:30 (11pp), 2013 September 20 doi:10.1088/0004-637X/775/1/30


# AN AZIMUTHAL ASYMMETRY IN THE LkH$\alpha$ 330 DISK

Andrea Isella[1], Laura M. Pérez[2], John M. Carpenter[1], Luca Ricci[1], Sean Andrews[3], and Katherine Rosenfeld[3]
[1] Department of Astronomy, California Institute of Technology, MC 249-17, Pasadena, CA 91125, USA; isella@astro.caltech.edu
[2] Jansky Fellow, National Radio Astronomy Observatory, Socorro, NM, USA
[3] Harvard-Smithsonian Center for Astrophysics, 60 Garden Street, Cambridge, MA 02138, USA
*Received 2013 April 18; accepted 2013 July 12; published 2013 August 30*

## ABSTRACT

Theory predicts that giant planets and low mass stellar companions shape circumstellar disks by opening annular gaps in the gas and dust spatial distribution. For more than a decade it has been debated whether this is the dominant process that leads to the formation of transitional disks. In this paper, we present millimeter-wave interferometric observations of the transitional disk around the young intermediate mass star LkH$\alpha$ 330. These observations reveal a lopsided ring in the 1.3 mm dust thermal emission characterized by a radius of about 100 AU and an azimuthal intensity variation of a factor of two. By comparing the observations with a Gaussian parametric model, we find that the observed asymmetry is consistent with a circular arc, that extends azimuthally by about 90° and emits about 1/3 of the total continuum flux at 1.3 mm. Hydrodynamic simulations show that this structure is similar to the azimuthal asymmetries in the disk surface density that might be produced by the dynamical interaction with unseen low mass companions orbiting within 70 AU from the central star. We argue that such asymmetries might lead to azimuthal variations in the millimeter-wave dust opacity and in the dust temperature, which will also affect the millimeter-wave continuum emission. Alternative explanations for the observed asymmetry that do not require the presence of companions cannot be ruled out with the existing data. Further observations of both the dust and molecular gas emission are required to derive firm conclusions on the origin of the asymmetry observed in the LkH$\alpha$ 330 disk.

*Key words:* planet–disk interactions – protoplanetary disks – submillimeter: planetary systems – techniques: interferometric

*Online-only material:* color figures

## 1. INTRODUCTION

Although it is generally accepted that planets form in disks around young stars, the evidence supporting this hypothesis is circumstantial. In 1989, measurements of the spectral energy distributions (SEDs) of young stellar systems revealed a family of objects characterized by little or none near- and mid-infrared excess, but higher luminosity at longer wavelengths (Strom et al. 1989). It was immediately recognized that the lack of infrared emission might be a sign of clearing of small dust grains from the inner disk, as previously predicted in the presence of forming giant planets (Lin & Papaloizou 1979). With the idea that these objects would be evolving to planetary systems, they were called transitional disks. In the last decade, infrared observations by the *Spitzer Space Telescope* revealed dozens of transitional disks (see, e.g., Cieza et al. 2012b; Currie & Sicilia-Aguilar 2011), which represent at least 15% of the total disk population (Muzerolle et al. 2010). However, it took almost two decades after their discovery to spatially resolve in the dust continuum emission the inner cavities predicted by SED models (Piétu et al. 2006).

Detections of companions orbiting within dust-depleted cavities have been obtained using aperture masking interferometric observations and speckle imaging at infrared wavelengths. In the case of CoKu Tau 4, the observations revealed that the cavity is due to a stellar mass companion orbiting at about 8 AU from the central star (Ireland & Kraus 2008). This result raised the possibility that transitional disks might be circumbinary disks. However, observations of T Cha, LkCa 15, and TW Hya suggest the presence of companions with masses below the deuterium burning limit (Huélamo et al. 2011; Kraus & Ireland 2012; Arnold et al. 2012).

Besides these few detections, crucial information on the nature of transitional disks has been obtained through spatially resolved observations of the disk emission at infrared and millimeter wavelengths. In particular, long baseline interferometric observations have revealed cavities in the (sub-)millimeter dust continuum emission (called millimeter cavities henceforth) that extend out to several tens of AU from the central star (Brown et al. 2008, 2012; Andrews et al. 2009, 2011; Hughes et al. 2009; Isella et al. 2010a, 2010b, 2012; Cieza et al. 2012a). In the case of SAO 206462, LkCa 15, PDS 70, and 2MASS J16042165–2130284, the millimeter cavities correspond to cavities in the near-infrared scattered light, and their sizes are in good agreement with the predictions of SED models (Thalmann et al. 2010; Muto et al. 2012; Dong et al. 2012; Mayama et al. 2012, respectively). However, some of the most extended millimeter cavities are not accompanied by a deficit in the near-infrared excess (Piétu et al. 2005; Isella et al. 2010b; Andrews et al. 2011) or contain a significant amount of molecular gas (Casassus et al. 2013; Dutrey et al. 2008; Isella et al. 2010b; Rosenfeld et al. 2012). Infrared and millimeter observations also reveal that disks characterized by large millimeter cavities can significantly deviate from central symmetry. For example, the disks around the Herbig Ae stars AB Aur, SAO 206462, and MWC 758, and HD 142527 show spiral arcs in the scattered light emission that have been interpreted as evidence of dynamical interactions by unseen low mass companions (Hashimoto et al. 2011; Muto et al. 2012; Grady et al. 2013). In the case of AB Aur, millimeter observations reveal an asymmetric ring of dust with a radius of about 150 AU and spiral arms in the CO (2–1) line emission that correspond to spiral arcs observed in scattered light (Tang et al. 2012; Fukagawa et al. 2004). Prominent asymmetries in the millimeter

emission have been also detected toward SAO 206462, MWC 758, and HD 142527, but their geometrical structure is not well constrained due to the limited angular resolution of existing observations (Ohashi 2008; Isella et al. 2010b; Andrews et al. 2011; Casassus et al. 2013). The spatially resolved observations of transitional disks obtained to date reveal structures that are much more complex than those suggested by SED models but still lack the angular resolution and sensitivity required to explain the broad range of observed properties.

In this paper, we present new CARMA observations of the 1.3 mm dust emission toward LkH$\alpha$ 330, a 3 Myr old, G3 pre-main-sequence star in the Perseus molecular cloud at a distance of 250 pc ($M_\star = 2.5\ M_\odot$; Osterloh & Beckwith 1995; Cohen & Kuhi 1979). Previous Submillimeter Array (SMA) observations of the 0.88 mm dust emission revealed that LkH$\alpha$ 330 is surrounded by a circumstellar disk inclined by about 35° with respect to the line of sight that extends out to at least 130 AU from the central star. These observations also revealed a millimeter cavity with a radius of 40 AU and a possible azimuthal asymmetry in the dust emission outside the cavity (Brown et al. 2008). Near-infrared Keck aperture masking observations exclude the presence of stellar mass companions at a projected separation larger than 40 mas, which corresponds to orbital radii between 10 AU and 13 AU at the distance of LkH$\alpha$ 330 and for a disk inclination of 35° (A. Kraus 2013, private communication). These observations leave open the possibility that the large millimeter cavity might be cleared by brown dwarfs or planetary size companions. More recent SMA observations revealed that the millimeter cavity is larger, about 70 AU in radius, than estimated by Brown et al. (2008), and that the overall dust emission can be explained reasonably well with a symmetric disk model Andrews et al. (2011). The CARMA observations presented in this paper achieve better image fidelity than previous SMA data, which allows us to derive firm conclusions on the presence of asymmetries in LkH$\alpha$ 330 disk.

The paper is organized as follows. The CARMA observations are presented in Section 2. In Section 3 we analyze the CARMA data, as well as the previously published SMA data, to constrain the geometrical properties of the asymmetries observed in the dust emission. In Section 4 we discuss the physical processes that can lead to the formation of azimuthal asymmetries in the dust emission. We present our conclusions in Section 5.

## 2. OBSERVATIONS

LkH$\alpha$ 330 was observed between 2008 December and 2009 January using the CARMA A and B array configurations, which provide baseline lengths in the range 82–1900 m. Receivers were tuned at the frequency of 230 GHz ($\lambda = 1.3$ mm) and the correlator was configured to use a total bandwidth of 4 GHz to maximize the sensitivity to the continuum. Atmospheric conditions during the observations were excellent, with zenith opacity $\tau_{230\,\mathrm{GHz}} < 0.15$ and rms noise phase coherence below 100 $\mu$m as measured on a 100 m baseline.

Data were calibrated using the Multichannel Image Reconstruction, Image Analysis and Display (MIRIAD) software package (Sault et al. 1995). The radio galaxy 3C111, separated by 8.°7 from LkH$\alpha$ 330, was observed every 7 minutes to measure the complex antenna gains and system bandpass shape. Further, on the longest baselines, the CARMA Paired Antenna Calibration System (Pérez et al. 2010), was applied to derive antenna gains on a timescale of 10 s. By simultaneous observations of a nearby point source we estimate that the phase decoherence after antenna gain calibration corresponds to a seeing of less than 0.″05. Absolute flux density calibration was obtained by observing Uranus, and by comparing the flux density of 3C111 with almost simultaneous SMA observations; the flux density uncertainty is estimated to be 10%.

We also analyze SMA observations of the 0.88 mm dust continuum emission measured toward LkH$\alpha$ 330 previously published by Brown et al. (2008) and Andrews et al. (2011). The details of the adopted receiver and the correlator configuration are described in these two works and will not be repeated here. The SMA observations were obtained with the "very extended" array configuration on 2006 November and with the compact configuration on 2010 November. Once combined, the data provide baseline lengths between 8 m and 509 m. The SMA data were calibrated using the MIR software package. The bandpass response of the system was set by observing the nearby quasars 3C273, 3C454.3, and 3C84, while the complex antenna-based gain were calibrated by observing 3C111. The absolute flux scale of the visibilities was derived by observing Uranus and Titan, resulting in a systematic uncertainty of about 10%.

To properly combine observations taken at different epochs, we shifted the phase center of each track by the known stellar proper motion. We adopted the J2000 coordinates and proper motion from the UCAC4 catalog (Zacharias et al. 2013): R.A. = $03^{\mathrm{h}}45^{\mathrm{m}}48^{\mathrm{s}}.282 \pm 0.001$s, Decl. = $+32°24'11''.85 \pm 0''.02$ pmR.A. = $3.9 \pm 2.0$ mas yr$^{-1}$, and pmDecl. = $-6.5 \pm 2.1$ mas yr$^{-1}$. The SMA tracks obtained in the "very extended" and compact array configurations were corrected by assuming a time baseline of 6.8 yr and 10.8 yr, respectively. The time baselines for the CARMA A and B array configuration observations are 8.9 yr and 9.0 yr, respectively. The same time baselines were used to derive the uncertainty on the modern position of the star due both to the errors on the J2000 coordinates and on the proper motion. We calculate that the absolute uncertainty on the stellar position at the time of the observations varies between 35 mas and 40 mas.

Errors in the centering position of each track might in principle produce spurious asymmetric structures in the image resulting from their combination. However, since the CARMA observations were obtained only one month apart, the error in the relative centering position due to the stellar proper motion is less than 1 mas. In the case of SMA data, the observations are separated by 4 yr, which lead to a possible centering error of about 8 mas. In both cases, the centering errors should be much smaller than the angular resolution of the observations and should not significantly affect the morphology of the dust continuum emission.

## 3. MORPHOLOGY OF THE DUST EMISSION

### 3.1. Image Domain

Figure 1 presents the images of the LkH$\alpha$ 330 disk at the wavelengths of 1.3 mm and 0.88 mm as obtained with CARMA and SMA, respectively. The CARMA observations achieve an angular resolution of 0.″35, or a spatial resolution of 90 AU at the distance of the source, as obtained by applying natural weighting to the *uv* data. The SMA image has similar resolution with uniform weighting, which boosts the angular resolution by down-weighting the data obtained on the short spatial scales. The CARMA and SMA observations achieve a noise level of 0.5 mJy beam$^{-1}$ and 2.6 mJy beam$^{-1}$, respectively.

Flux densities integrated on a circular aperture of 1.″5 in diameter are $53 \pm 2$ mJy and $204 \pm 8$ mJy at 1.3 mm and

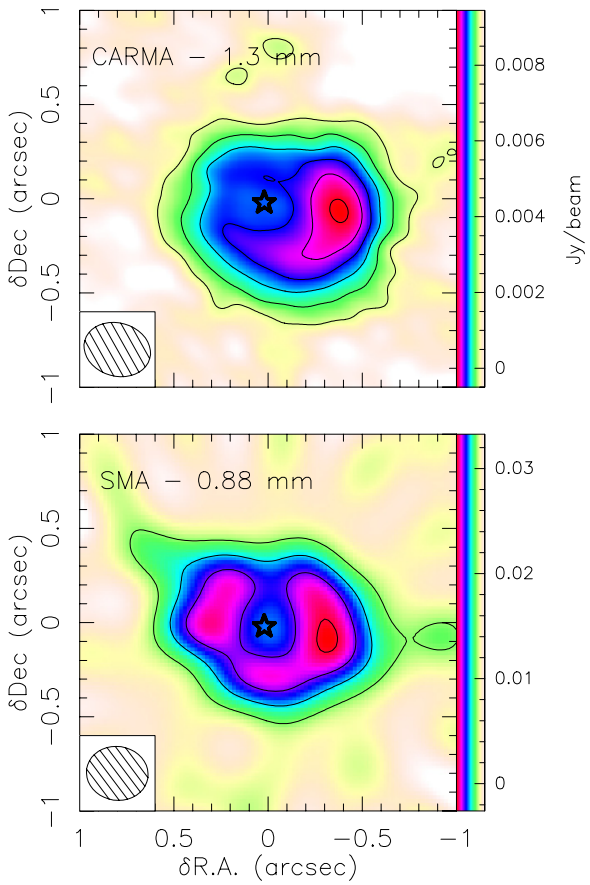


**Figure 1.** Maps of the continuum emission observed toward LkH$\alpha$ 330 at the wavelength of 1.3 mm (top) and 0.88 mm (bottom). The two maps have a similar angular resolution of about 0.″35. The intensity contours are spaced by three times the noise level, where the noise level is 0.5 mJy beam$^{-1}$ and 2.6 mJy beam$^{-1}$ in the top and bottom panel, respectively. The position of the central star is indicated with the star symbol.

(A color version of this figure is available in the online journal.)

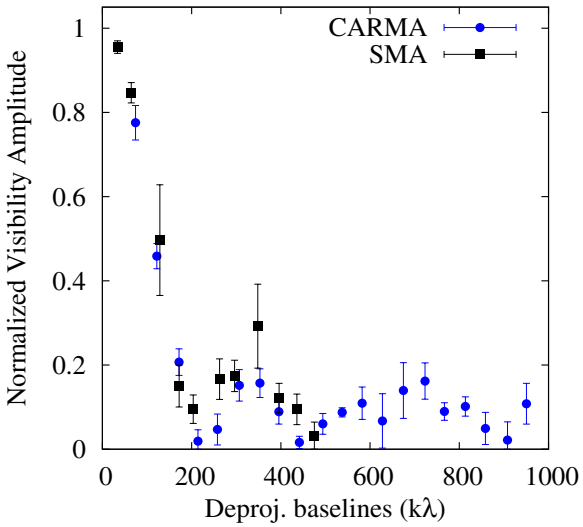


**Figure 2.** Normalized visibility amplitude vs. deprojected baseline. CARMA and SMA data are shown with circles and squares, respectively.

(A color version of this figure is available in the online journal.)

0.88 mm, respectively, where the uncertainties reflect random noise only. The spectral index measured between 0.88 mm and 1.3 mm is 3.6 ± 0.5 (random noise) ± 1.0 (flux calibration), which is consistent within the large uncertainty with the mean value of 2.6 measured toward nearby circumstellar disks (Ricci et al. 2010).

The CARMA and SMA maps show similar features: the dust emission from the disk extends for about 1″ in diameter (250 AU), and has a local minimum at the stellar position, which is indicated by the star symbol in Figure 1 (the size of the symbol is the same as the uncertainty on the position of the star). Both maps reveal that the west side of the disk is brighter than the east side, though this asymmetry is more evident at 1.3 mm than at 0.88 mm. The 1.3 mm intensity has a maximum of 9.3 ± 0.5 mJy beam$^{-1}$ located 0.″4 westward from the star, while the value at the symmetric point is only 2.8 ± 0.5 mJy beam$^{-1}$. The integrated flux density westward and eastward of the star is 35 ± 1 mJy and 18 ± 1 mJy, respectively. At 0.88 mm, the integrated flux densities for the west and east side of the disk are 109 ± 4 mJy and 94 ± 4 mJy, respectively, with a peak of 33.0 ± 2.6 mJy beam$^{-1}$ in the west side and 26.1 ± 2.6 mJy beam$^{-1}$ in the symmetric position.

### 3.2. Fourier Domain

A better understanding of the morphology of the dust emission observed toward LkH$\alpha$ 330 can be achieved by inspecting the complex visibilities, which, contrary to the intensity maps, are not affected by the synthesized beam smoothing and by possible artifacts introduced during the image deconvolution process.

Figure 2 shows the circularly averaged CARMA and SMA visibility amplitude versus the baseline length, where this latter quantity has been deprojected assuming a disk inclination of 35° and a position angle of 80° as derived by Andrews et al. (2011). To allow a comparison between CARMA and SMA data, the visibility amplitude has been normalized by the integrated flux density at the respective wavelengths.

The visibility profile drops to zero at about 200 kλ, implying that the emission is resolved on angular scales of about 1″. The presence of two additional nulls, located at 450 kλ and 900 kλ, respectively, indicate that the surface brightness is characterized by sharp radial variations. Andrews et al. (2011) modeled the SMA observations with a circular symmetric inclined disk characterized by a partially dust-depleted cavity of 70 AU in radius. In this model, the dust surface density has a discontinuity at the outer cavity radius, which produces the first two lobes of the visibility profile. For the rest of the paper we will assume this as a reference disk model and will focus the discussion on the asymmetry observed in the dust emission.

While the visibility amplitude probes the angular scales of the observed emission, the imaginary part of the visibility (called imaginary visibility henceforth) provides information about its symmetry properties with respect to the phase center of the observations, i.e., the position in the sky at which the telescope was pointed. The Fourier transform has the property that a purely real even function, such as a two-dimensional (2D) centro-symmetric disk surface brightness, maps in a purely real function. Therefore, nonzero imaginary visibilities, which corresponds to the imaginary part of Fourier transform of the disk surface brightness, indicate the presence of an asymmetry with respect to the phase center of the observations, which, in the case of LkH$\alpha$ 330 observations, corresponds to the expected position of the star corrected for the stellar proper motion (see Section 2).

Figure 3 presents the *uv* coverage achieved by CARMA observations and the imaginary visibilities along $u$ and $v$, as calculated by binning the data every 80 kλ. Although the

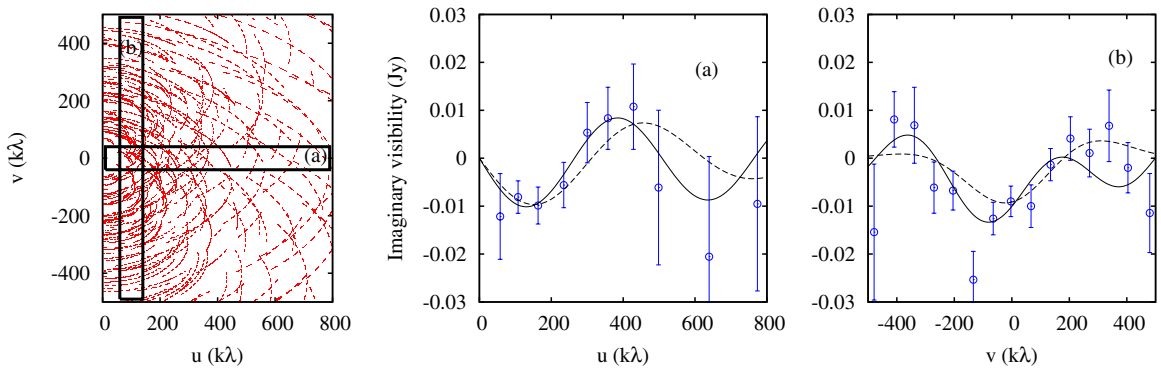


**Figure 3.** Left: coverage of the *uv* plane of the CARMA observations of LkH$\alpha$ 330. Center: imaginary visibilities measured on the *uv* plane region labeled as (a). Open circles indicate values averaged between −40 kλ and 40 kλ along $v$ and every 80 kλ along $u$. Right: imaginary part of the correlated flux measured on the *uv* plane region labeled as (b), averaged from 60 kλ and 140 kλ along $u$ and every 80 kλ along $v$. The dashed and solid black curves show the imaginary visibilities of the single- and two-component best fit models, whose properties are listed in Table 1.

(A color version of this figure is available in the online journal.)

**Table 1**
Gaussian Model

| | $x_0$ (″)[a] | $y_0$ (″) | $\sigma_{\rm maj}$ (″) | $\sigma_{\rm min}$ (″) | $F$ (Jy) | $\theta$ (°) | $\chi^2_r$ |
|---|---|---|---|---|---|---|---|
| Single-component best fit model | | | | | | | 1.09 |
| g1 | $0.37 \pm 0.03$ | $-0.20 \pm 0.03$ | $0.16 \pm 0.06$ | $<0.05$ | $0.011 \pm 0.002$ | $70 \pm 5$ | |
| Two-component best fit model | | | | | | | 1.03 |
| g1 | $0.40 \pm 0.03$ | $-0.11 \pm 0.02$ | $0.14 \pm 0.05$ | $<0.05$ | $0.009 \pm 0.002$ | $88 \pm 5$ | |
| g2 | $0.05 \pm 0.03$ | $-0.43 \pm 0.03$ | $0.21 \pm 0.07$ | $<0.05$ | $0.007 \pm 0.002$ | $8 \pm 5$ | |

**Note.** [a] The $x$ coordinate is positive toward west, i.e., $dx = -d$ R.A.

following analysis makes use of all the *uv* data, for sake of clarity we only show the values measured inside the rectangles (a) and (b). In these regions, the imaginary visibilities clearly deviate from zero, and oscillate around zero reaching maximum values around 15 mJy. This suggests that about 30% of the integrated flux arises from asymmetric structures.

In the following, we analyze the imaginary visibilities to constrain the geometrical properties of the asymmetries in the disk emission. To this end, we assume that any arbitrary asymmetric structure in the image domain can be expressed as a combination of 2D Gaussian functions,

$$g(x, y) = A \times \exp\left\{-\frac{[(x - x_0)\cos\theta + (y - y_0)\sin\theta]^2}{2\sigma^2_{\rm maj}}\right\} \times \exp\left\{-\frac{[(x - x_0)\sin\theta - (y - y_0)\cos\theta]^2}{2\sigma^2_{\rm min}}\right\}, \quad (1)$$

where $A$ is the intensity at the central position $(x_0, y_0)$, $\sigma_{\rm maj}$ and $\sigma_{\rm min}$ are the dispersions along the major and minor axis, and $\theta$ is the position angle of the major axis with respect of the $x$-axis measured counter-clockwise. The Fourier transform of Equation (1) can be calculated analytically (see the Appendix), and its imaginary part can be expressed as

$$\Im(G(u, v)) = A \times 2\pi\sigma_{\rm maj}\sigma_{\rm min} \times \sin[-2\pi(ux_0 + vy_0)] \times \exp\left\{-2\pi^2\left[(u\cos\theta + v\sin\theta)^2\sigma^2_{\rm maj} + (-u\sin\theta + v\cos\theta)^2\sigma^2_{\rm min}\right]\right\}. \quad (2)$$

To analyze the observations, we start by assuming a single Gaussian component and calculate the best fit values for $x_0$, $y_0$, $\sigma_x$, $\sigma_x$, $A$, $\theta$, as well as the corresponding uncertainties, through a nonlinear least-squares Marquardt–Levenberg fit of the imaginary visibilities measured by CARMA. If the reduced $\chi^2$, $\chi^2_r$, obtained with a single component is significantly larger than unity, we repeat the fitting procedure assuming two Gaussian components. We continue adding Gaussian components until $\Delta\chi^2_r = \chi^2_r - 1$ is less than the value corresponding to the 99% confidence level agreement between the model and the observations. This latter value depends on the number of degrees of freedom in the model fitting, as well as on the number of visibilities, and, in the case of CARMA observations, is 0.04, 0.07, and 0.1 for one, two, and three Gaussian components, respectively.[4]

We find two Gaussian components are required to obtain a good fit of the imaginary visibilities ($\chi^2_r = 1.03$), while the best fit model with a single component is outside the 99% confidence level ($\chi^2_r = 1.09$). The properties of both the single- and two-component best fit models are summarized in Table 1, while Figure 3 shows the comparison in the Fourier space between the best fit models and the observations. As a check of the fitting procedure, we decomposed the observed 1.3 mm dust emission into its asymmetric and symmetric components. Figure 4 shows the 1.3 mm CARMA observations, the maps of single- and two-component best fit models, and the residual maps obtained by subtracting in the Fourier space the models from the observations. The residual map for the single-component model shows a faint residual asymmetry in the south part of the disk, which is accounted for by the two-component

[4] These values are calculated as $\Delta\chi^2/(N-p)$ where $N = 282$ is the number of visibilities, $p = 6$, 12, and 18 is the number of free parameters corresponding to one, two, and three Gaussian components, respectively, and $\Delta\chi^2 = 10.64$, 18.55, and 25.99 is the value corresponding to 99% confidence level in the case of 6, 12, and 18 free parameters.

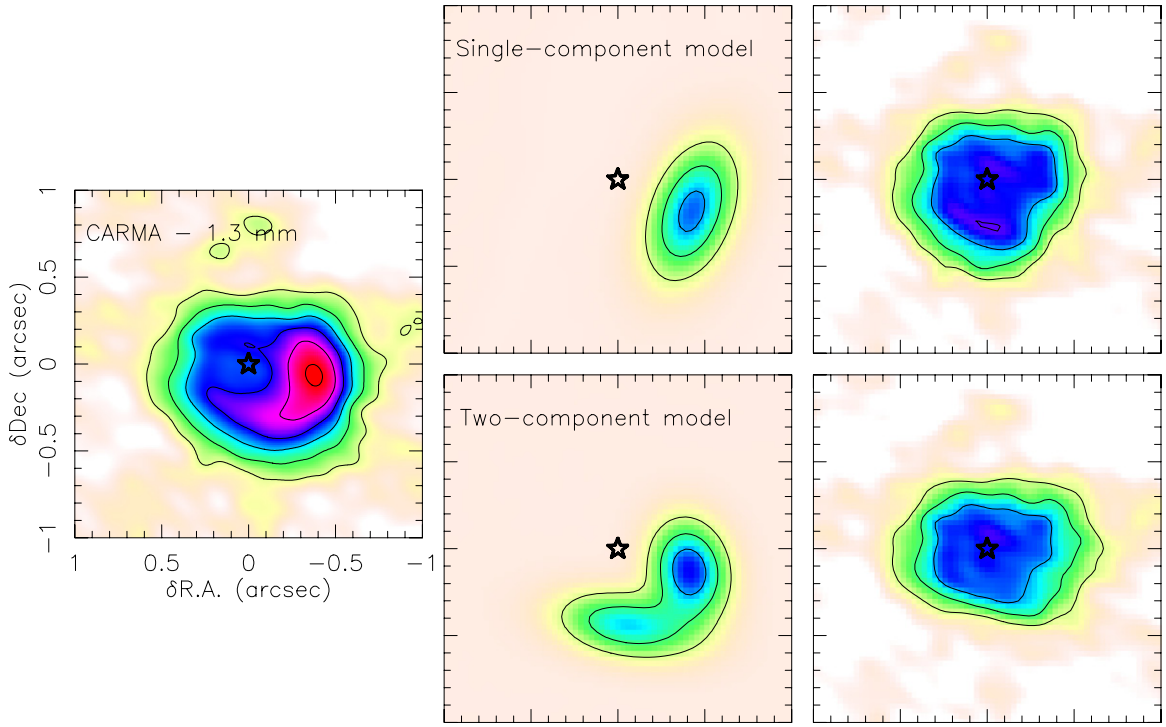


**Figure 4.** Left: map of the dust continuum emission observed by CARMA at a wavelength of 1.3 mm toward LkH$\alpha$ 330. The color scale and the contours are as in Figure 1. Center: maps of the best fit models for the imaginary visibilities. Right: maps of the residuals obtained by subtracting in the Fourier space the best fit model for the imaginary visibilities from the observations. The single- and two-component best fit models are shown in the top and bottom panels, respectively.
(A color version of this figure is available in the online journal.)

best fit model. The appearance of asymmetries in the residual map is consistent with the $\chi^2$ analysis, giving us confidence on the procedure employed to identify asymmetric structures in the LkH$\alpha$ 330 disk.

The two Gaussian components that fit the imaginary visibilities have integrated fluxes of 9 mJy and 7 mJy, respectively, which account for about 30% of the total flux density measured at 1.3 mm. They are centered at a radius of about 0.″42 from the central star, which corresponds to a separation of about 100 AU, and are oriented so that the minor axis is aligned along the radial direction and the major axis is tangential to a circle of 100 AU in radius. Along the major axis, they extend by more than 70 AU, while along the minor axis they appear to be spatially unresolved. This sets the upper limit for their radial extent to about 25 AU.

Figure 5 shows the *uv* coverage achieved by the SMA observations, as well as the imaginary visibilities calculated as in the case of the CARMA data. We find that, due to the sparse *uv* coverage for spatial frequencies larger than 100 $k\lambda$, the SMA data provide poor constraints on disk asymmetries. More specifically, the SMA imaginary visibilities are consistent within 99% confidence level with both a symmetric model for the dust emission and with the single- and two-component best fit Gaussian models derived from the CARMA observations. These latter are shown with dashed and solid black lines, respectively, and have been calculated by assuming an optically thin emission with a spectral index $\alpha = 3.6$. Lower values of $\alpha$ will lead to a lower flux of the asymmetric structures at 0.88 mm and therefore to an even fainter signal in the imaginary visibilities. By contrast, the imaginary visibilities of the asymmetries inferred at 1.3 mm would be incompatible with the measured values at 0.88 mm for $\alpha > 4$. This is, however, an unlucky case since it would imply a dust opacity slope $\beta$ larger than 2.

## 4. DISCUSSION

Models of the SMA observations of LkH$\alpha$ 330 find that the 0.88 mm dust thermal emission is optically thin, with a maximum optical depth of about 0.3 at the outer edge of the dust-depleted cavity located at 70 AU from the central star (Andrews et al. 2011). Since dust opacity of typical interstellar grains decreases with the wavelength (i.e., $\beta \geqslant 0$; Draine 2006), then the 1.3 mm dust emission from LkH$\alpha$ disk should also by optically thin. We can therefore express it as

$$I_\nu(r,\theta) \propto B_\nu(T(r,\theta)) \times k_\nu(r,\theta) \times \Sigma_g(r,\theta), \qquad (3)$$

where $T$ is the temperature of the disk mid plane, $k_\nu$ is the dust opacity *per gram of gas*, and $\Sigma_g$ is the gas disk surface density. The asymmetries observed in the dust emission can therefore be caused by the deviation from the central symmetry of the disk density, temperature, and/or opacity. In the following we discuss possible physical effects that might lead to such variations.

### 4.1. Azimuthal Density Perturbations Due to the Disk–Planet Interaction

Planets embedded in nearby circumstellar disks are too faint to be directly observed at millimeter wavelengths. However, planets more massive than Jupiter will gravitationally interact with the surrounding circumstellar material, leading to the formation of annular gaps and density waves in the gas density distribution around the planetary orbit (Lin & Papaloizou 1986; Bryden et al. 1999; Rafikov 2002; Crida et al. 2006). These structures might have spatial scales of tens of AU and can be observed by existing telescopes, therefore providing an indirect tool to study the formation of planets.

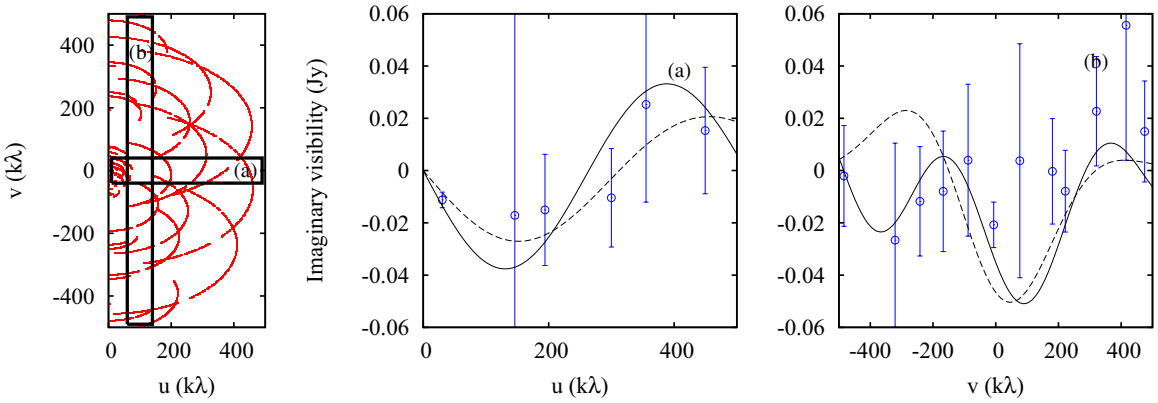


**Figure 5.** Left: coverage of the *uv* plane of the SMA observations of LkH$\alpha$ 330. Center and right: imaginary visibilities measured as in Figure 3. The dashed and solid black curves show the imaginary visibilities of the single- and two-component best fit models, where the flux of the asymmetric components has been scaled to account for the difference in wavelength by assuming a spectral index $\alpha = 3.6$, as measured from the integrated fluxes at 0.88 mm and 1.3 mm.

(A color version of this figure is available in the online journal.)

Dynamical clearing by giant planets has been proposed as a possible mechanism to explain the lack of near-infrared emission and the presence of millimeter cavities toward transitional disks (Brown et al. 2008; Isella et al. 2010b; Andrews et al. 2011; Isella et al. 2012). Dodson-Robinson & Salyk (2011, hereafter DS11) suggest that planetary systems composed of two or more giant planets might naturally explain millimeter cavities larger than 15 AU. Similar results are found by Zhu et al. (2011), who also argue that multiple giant planets would lead to a mass accretion rate onto the central star which is orders of magnitude lower than that measured toward transitional disks with large millimeter cavities. In a following paper, Zhu et al. (2012) suggest that one single giant planet orbiting close to the outer edge of the millimeter cavity might be sufficient to explain the cavity diameter if millimeter size grains are trapped in the pressure bump that forms at the outer edge of the dust-depleted cavity (see also Pinilla et al. 2012).

While it is generally accepted that one or more giant planets can lead to large millimeter cavities, the role of the disk–planet interaction in creating azimuthal asymmetries in the disk emission has not been explored in great detail. In the case of a single Jupiter mass planet, de Val-Borro et al. (2007) find that large-scale vortices can form at the outer edge of the annular gap cleared by the planet as a result of Rossby wave instabilities. Azimuthal asymmetries in the disk surface density also appear in hydrodynamic simulations with multiple giant planets by DS11, but it remains to be shown if they are a general outcome of the disk–planet interaction, how they depend on the orbital parameters and mass of the planets, and how they will influence the millimeter-wave dust thermal emission.

To address these questions, we have performed hydrodynamic simulations using FARGO, a publicly available, polar grid-based 2D hydrodynamic code expressly designed to study the disk–planet interaction (Masset 2000). To date, FARGO has been employed to investigate the radial migration of planets in viscous disks (Masset 2000, 2001, 2002; Masset & Papaloizou 2003; Masset & Ogilvie 2004; Masset et al. 2006; Masset & Casoli 2009, 2010; Crida et al. 2007) and the effects of circumplanetary disks on planet migration (Crida et al. 2009). FARGO was also employed to study the opening of annular gaps in the disk surface density due to the gravitational field of a planet (Crida et al. 2006) and to check whether forming planetary systems might be able to open cavities as large as of those observed in transitional disks (DS11; Zhu et al. 2011).

The simulations are performed adopting a procedure similar to that described in DS11. First, we generate a planetary system that is able to carve a cavity characterized by an outer radius of 70 AU, as observed in the LkH$\alpha$ 330 disk (Andrews et al. 2011). We assume that the size of the gap opened by the gravitational torque exerted by a planet on the disk is five times the planet Hill radius, defined as $R_H = R_p(M_p/3\,M_\star)^{1/3}$, where $R_p$ and $M_p$ are the planet's orbital radius and mass, respectively (see, e.g., Bryden et al. 1999). To create a cavity of 70 AU in radius, the outermost planet should therefore have an orbital radius equal to 70 AU $\times\,(1 + 2.5(M_p/3\,M_\star)^{1/3})^{-1}$. Gaps created by multiple planets with the same mass will overlap if their orbital radii are separated by $\Delta r_{ij} = 2.5(r_i + r_j)(M_p/3M_\star)^{1/3}$. In our reference model, we assume a planet mass of 5 $M_J$ and, following the previous relations, we place four planets at orbital distances of 55 AU, 34 AU, 21 AU, and 13 AU to have a cavity from 10 AU to 70 AU. We anticipate here that the mass and number of planets do not affect the main results of our analysis.

The disk properties are as in DS11: we assume a constant aspect ratio $h_p/r = 0.05$, where $h_p$ is the disk pressure scale height; the disk surface density is expressed by a power law $\Sigma \propto r^{-1}$; the disk viscosity is parameterized using the Shakura–Sunyaev $\alpha$ parameter and we assume $\alpha = 0.002$. The inner and outer radius of our simulations are set to 1 AU and 160 AU, respectively, and we choose the surface density normalization constant so that the disk mass is 0.03 $M_\odot$, i.e., similar to that inferred from SMA observations. Finally, as in DS11, we allow the planets to feel the torque from the disk after they have opened a gap in the disk surface density. This artificially suppresses the Type I migration which is not properly described by the FARGO code and would cause rapid inward migration of the planets.

Figure 6 shows the gas surface density map after 100, 1000, and 2000 orbits of the outermost planets, which corresponds to about $5 \times 10^4$ yr, $5 \times 10^5$ yr, and $10^6$ yr, respectively. A cavity of about 70 AU in radius is created after a few orbits of the outermost planet. Between about 70 AU and 90 AU, azimuthal asymmetries with the shape of circular arcs develop. After $5 \times 10^4$ yr, the surface density at 80 AU from the star varies azimuthally by more than a factor of two, from about 18 g cm$^{-2}$ to about 8 g cm$^{-2}$. This density contrast has about the same amplitude of the intensity contrast measured in the 1.3 mm dust emission, as discussed in Section 2. In addition, the bright circular arcs have roughly Gaussian density profiles both

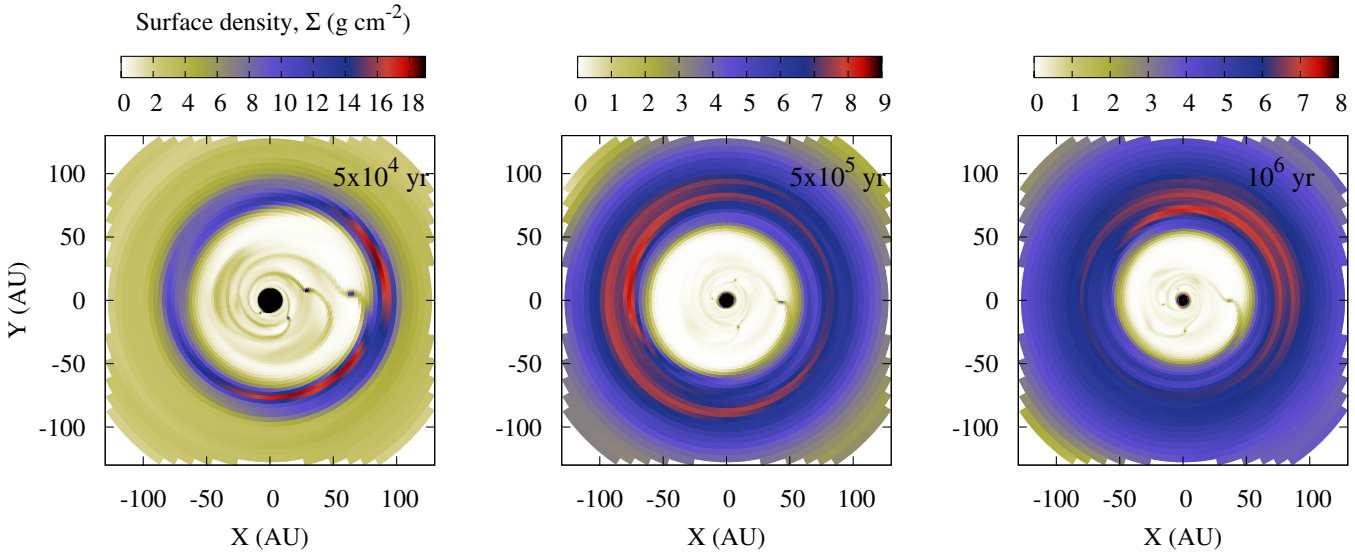


**Figure 6.** Hydrodynamic simulations of the perturbing effects of a planetary systems composed by four 5 $M_J$ planets on the disk surface density. The three panels from the left to the right show snapshots of the surface density after $5 \times 10^4$ yr, $5 \times 10^5$ yr, and $10^6$ yr, respectively.

(A color version of this figure is available in the online journal.)

radially and azimuthally with dispersions of 10 AU and 50 AU, respectively, which are similar to size of the asymmetries derived from the CARMA observations (see Section 3.2). Snapshots of the surface density at later ages show that the azimuthal asymmetries between 70 AU and 90 AU are persistent, although the density contrast decreases with time down to about 30% after $10^6$ yr. In the assumption that dust and gas are well coupled (we investigate this assumption in the next section), these simulations indicate that disk–planet interaction might naturally explain the morphology of the dust emission observed toward LkH$\alpha$ 330, and, if taken at face value, would suggest that an azimuthal contrast of about 2 in the millimeter dust emission might result from a recent ($<10^4$ yr) episode of planet formation.

However, the geometrical properties and the temporal evolution of the azimuthal asymmetries observed in hydrodynamic simulations might depend on a number of unknown, or poorly constrained parameters, such as the mass, the orbital radius, and number of planets, and the disk viscosity. An extensive exploration of the parameter space is therefore required to constrain the properties of possible companions orbiting LkH$\alpha$ 330 from the existing millimeter-wave observations. Such a study requires a large amount of computational time, which goes beyond our present computational capabilities and the scope of this work. In this paper, we limit our analysis to investigate whether the formation of azimuthal asymmetries in the disk surface density is a general outcome of the disk–planet interaction or, on the contrary, requires a fine tuning of the model parameters. To this end, we performed short ($10^4$ yr) hydrodynamic simulations using FARGO, in which we explored cases with one, two, and three planets characterized by masses between 3 $M_J$ and 10 $M_J$, and deployed so that the outer edge of the cleared cavities is located at about 70 AU as derived for LkH$\alpha$ 330. We varied the disk viscosity from $\alpha = 0.002$ and $\alpha = 0.02$, and changed the disk aspect ratio $h_p/r$ to account for a possible flaring geometry. In total we performed about 20 simulations. In all these cases, we observed that the disk–planet interaction leads to large-scale azimuthal asymmetries in the disk surface density between 70 AU and 90 AU from the central star. At the end of our simulations, i.e., after about $10^4$ yr, the density contrast at 80 AU varies azimuthally between a few percent to almost a factor of 10. The largest variations are observed in simulations with planets of 10 $M_J$ and low disk viscosity. Furthermore, we find that the azimuthal asymmetries are fainter and disappear in a shorter timescale in the case of high disk viscosity. These preliminary results (a more extensive exploration of the parameter space will be presented in a future paper) suggest that wide separation companions more massive than a few Jupiter masses might quite naturally explain the morphology of the dust emission observed toward LkH$\alpha$ 330, while less massive planets might not produce sufficiently strong asymmetries.

A recent direct-imaging survey has found that less than 20% of debris disk stars have a planet more massive than 3 $M_J$ beyond 10 AU (Wahhaj et al. 2013), suggesting that planetary systems like those proposed above are rare. However, circumstellar disks characterized by cavities larger than 15 AU are also rare, with a frequency less that 10% among the entire disk population (Andrews et al. 2011). The paucity of wide separation massive planets is therefore not in contrast with the suggested explanation for the morphology of LkH$\alpha$ 330 disk.

### *4.2. Azimuthal Density Perturbations Due to Disk Instabilities*

Rossby wave and baroclinic instabilities have been proposed as a possible mechanism to form lopsided asymmetries in the millimeter dust continuum emission without the need of companions (Klahr & Bodenheimer 2003; Wolf & Klahr 2002).

Regály et al. (2012) suggested that a large-scale vortex triggered by Rossby wave instability might be responsible for the asymmetry observed in the LkH$\alpha$ 330 dust continuum emission at 0.88 mm (Brown et al. 2008). In their model, the instability is triggered by a discontinuity in the disk viscosity due to the transition from a magnetorotational instability (MRI) dead-zone to an MRI active zone. We note that this hypothesis faces two major problems. First, the dead-zone should extend up to a distance of 70 AU from the central star, which is much larger than the extent predicted by theoretical models (see, e.g., the review by Armitage 2011). Second, Rossby wave instabilities

do not necessarily lead to a depletion of gas and dust inside the dead-zone region. The gas depletion preferentially happens in the active disk region, i.e., at distances larger than 70 AU, as the gas migrates inward and it is trapped into the vortex (see Figure 4 of Regály's paper). This model then may not explain the lack of infrared excess and the spatially resolved observations at millimeter wavelengths. A possible work around is that millimeter-size particles might be trapped in the vortex located at the outer edge of the dead-zone, resulting in a dust filtration process similar to that discussed by Zhu et al. (2012). This would lead to a reduced millimeter-wave dust opacity inside the dead-zone. However, dust particles smaller that about 1 $\mu$m might remain coupled to the gas and produce a significant amount of near-infrared emission.

Circumstellar disks heated by the central star are characterized by a radial gradient in the disk temperature which makes them prone to baroclinic instabilities (Raettig et al. 2013). Earlier 3D numerical simulations, which were characterized by a very small radial dynamic range, have shown that baroclinic instabilities lead to the formation of anticyclonic vortices, which might eventually merge and produce azimuthal structure similar to that observed toward LkH$\alpha$ 330 (Klahr & Bodenheimer 2003). In the last 10 yr, several theoretical investigations have expanded on this result to study the formation and evolution of vortices in rotating circumstellar disks, sometimes leading to controversial results (see, e.g., Johnson & Gammie 2006). Although a 3D model that covers the radial extent of a disk, i.e., a few hundred AU, is still missing, the most recent simulations confirm that vortices induced by baroclinic instabilities can form and survive for several hundred orbits (e.g., Petersen et al. 2007a, 2007b; Lesur & Papaloizou 2010; Raettig et al. 2013). However, it has not yet been explored whether this process can produce vortices in the outer regions of circumstellar disks, where baroclinic instabilities might not exist due to the fact that disks are almost isothermal in the radial direction.

### 4.3. Azimuthal Variations in the Dust Opacity

Equation (3) shows that azimuthal variations in the millimeter-wave dust emission can also result from azimuthal variations in the dust opacity. This might be the case if, for example, large dust grains are trapped in maxima of the gas pressure caused by local enhancements in the gas density. This process has been suggested to be involved in the formation of planetesimals, and it has been proposed as a possible solution for the radial drift problem of large particles in a turbulent disk (Pinilla et al. 2012). More recently, Birnstiel et al. (2013) have studied the dust trapping caused by azimuthal asymmetries in the gas surface density that might result, for example, from disk–planet interactions. They find that, if the density asymmetries are long-lived in the gas corotating rest frame, even weak variations of the order of 10% in the azimuthal gas density can lead to a large concentration of millimeter-size dust grains toward the peak of the gas density. Since the dust opacity at millimeter wavelengths is dominated by millimeter-size particles, dust trapping might therefore be a dominant process in the formation of asymmetries in the millimeter-wave dust continuum emission (van der Marel et al. 2013).

The efficiency of dust trapping depends critically on the stability of the pressure bumps and on the timescale required to concentrate particles. The stability of pressure bumps created by the disk–planet interaction can be investigated by analyzing the temporal evolution of the azimuthal gas asymmetries as calculated using FARGO. For the reference model shown in Figure 6, three phases can be identified. The initial phase lasts for about $10^4$ yr, and is very dynamic. Azimuthal asymmetries form and merge on a few orbital timescales, and no clear rotational pattern can be identified. A second phase starts after about $10^4$ yr, when a main lopsided asymmetry appears outside the gas-depleted cavity at an orbital radius of about 80 AU. The rotational velocity of this structure is initially about 70% of the local Keplerian velocity and increases with time up to 100% of the Keplerian velocity after about $10^5$ yr. In the third phase, which lasts from $10^5$ yr to the end of the simulation at about $10^6$ yr, the lopsided asymmetry is co-rotating with the local gas at Keplerian speed. These results suggest that planet-induced asymmetries might be stable for a long time.

Following Birnstiel et al. (2013), dust particles can be concentrated around gas pressure maxima only if $\mathrm{St} \geqslant \alpha$, where $\mathrm{St} \simeq \rho_s a/\Sigma_g$ is the Stoke number of a spherical dust grain of radius $a$ and internal density $\rho_s$, $\Sigma_g$ is the local gas surface density, and $\alpha$ is the Shakura–Sunyaev viscosity parameter. For $\alpha = 10^{-3}$–$10^{-2}$ (Armitage 2011, and references therein) and $\rho_s = 2\,\mathrm{g\,cm^{-3}}$ (Pollack et al. 1994), the concentration of millimeter-size dust grains therefore requires surface densities less than 20–200 $\mathrm{g\,cm^{-2}}$. This condition is generally satisfied in the outer regions of circumstellar disks (see, e.g., Isella et al. 2009). The timescale required to concentrate the dust grains can then be expressed as

$$\tau_c \sim \frac{1}{\rho_s a}\left(\frac{1}{\Sigma_g^{\min}} - \frac{1}{\Sigma_g^{\max}}\right)^{-1}\left(\frac{h_p}{r}\right)^{-2}\frac{2\pi}{\Omega_k}, \qquad (4)$$

where $\Omega_k$ is the angular Keplerian velocity, and $\Sigma_g^{\min}$ and $\Sigma_g^{\max}$ are the minimum and maximum values of the gas disk surface density at the orbital radius $r$. In the specific case of the LkH$\alpha$ 330, we calculate that the timescale to concentrate dust grains of 1 mm and 1 cm at a distance of 80 AU from the central star would be of about 10 Myr and 1 Myr, respectively, for $\Sigma_g^{\min} = 8\,\mathrm{g\,cm^{-2}}$, $\Sigma_g^{\max} = 18\,\mathrm{g\,cm^{-2}}$, and $h_p/r = 0.05$ as in the hydrodynamic simulations shown in the left panel of Figure 6. Although these estimates might be uncertain by a factor of several due to the uncertainty on the gas surface density, they suggest that the concentration of large grains in LkH$\alpha$ 330 outer disk might require a temporal scale comparable with the age of the stellar system.

As proposed by Birnstiel et al. (2013), spatially resolved observations of the dust thermal emission at millimeter and centimeter wavelengths will measure azimuthal variations in the spectral index of the dust thermal emission, and constrain the spatial distribution of dust grains with different sizes (see, e.g., Pérez et al. 2012). In addition, ALMA observations of optically thin molecular emission lines, such as, for example, the low-$J$ rotational transitions of CO isotopologues, might constrain the density and kinematics of the gas in LkH$\alpha$ 330 outer disk regions, and provide important information on the physical process that is causing the observed asymmetry.

### 4.4. Azimuthal Variations in the Dust Temperature

Fluctuations in the dust temperature might cause azimuthal variations in the millimeter-wave dust emission even in the case in which the dust opacity and density are symmetric. In the case of a passive disk, i.e., a disk heated only by the central star, the temperature of the disk interior depends on the incident angle $\alpha_{\mathrm{inc}}$ of the stellar radiation on the disk surface, so that larger values of $\alpha_{\mathrm{inc}}$ lead to higher disk temperatures (see, e.g.,

Chiang & Goldreich 1997). Azimuthal fluctuations of the disk temperature can therefore happen if, for example, the disk is warped, or if one side of the disk is more flared than the other side, or if part of the outer disk lays in the shadow cast by some asymmetric structures in the inner disk. Such structures should have a scale of several AU, or tens of AU, to be able to affect the dust temperature across a large fraction of the disk far from the central star, and might therefore significantly differ from the small structures thought to be responsible of the short timescale variability observed in the disk mid-infrared emission (Morales-Calderón et al. 2012).

The presence of companions orbiting LkH$\alpha$ 330 inside the millimeter cavity can affect the dust temperature in several ways. A warped disk might originate if the orbits of the companions are misaligned with the disk plane, as has been suggested to explain the warped geometry of the $\beta$ Pic disk (see, e.g., Dawson et al. 2011). In addition, local variations of the disk flaring geometry might also occur at the inner and outer edges of the annular gaps cleared by the companions (Jang-Condell & Turner 2012). Finally, the azimuthal variations in the disk surface density discussed in Section 4.1 might also lead to variations in the dust temperature by changing the height of the disk surface. We investigated this latter point by performing radiative transfer calculations on the disk surface density provided by FARGO simulations by adopting the "two-layer" model discussed in Isella et al. (2009). We find that azimuthal fluctuations of a factor of two in the disk surface density might lead to variations in the disk mid plane temperature of about the same amplitude. However, the dependence of the disk temperature from the disk surface density is complex and needs to be investigated by adopting more accurate radiative transfer models.

Finally, we note that asymmetries in the dust temperature might also occur if the disk is warped by a close stellar encounter (Larwood & Kalas 2001), or, for example, if transient density fluctuations in the inner disk, e.g., the vortices that might originate from Rossby wave instabilities at the outer edge of MRI dead-zone (Lyra & Mac Low 2012), cast a shadow on the outer disk, temporarily reducing the amount of stellar radiation that heats the disk mid plane.

Asymmetries in the LkH$\alpha$ 330 disk temperature can be measured by mapping the disk emission in optically thick molecular lines, such those corresponding to the low-$J$ transitions of $^{12}$CO or CS. These observations are sensitive to the temperature of the disk layer at a depth of $\tau \sim 1$, and, when combined with observations of optically thin lines, would enable us to investigate whether the asymmetry observed in the millimeter-wave continuum emission toward LkH$\alpha$ 330 is mainly caused by variations in the dust temperature, density, or opacity.

## 5. CONCLUSIONS

We present CARMA interferometric observations of the pre-main-sequence star LkH$\alpha$ 330 that reveal a lopsided ring in the 1.3 mm dust continuum emission. The ring has radius of about 100 AU and an azimuthal intensity variation of a factor of two. By comparing the imaginary visibilities with parametric Gaussian models, we find that the asymmetry in the dust emission traces a narrow circular arc, which extends in the azimuthal direction by about 90° and accounts for about 1/3 of the total disk flux at 1.3 mm.

Disk–planet interaction has been suggested as a possible mechanism to create large millimeter cavities, as that observed in the LkH$\alpha$ 330 disk. We perform hydrodynamic simulations using FARGO to investigate whether this process might also explain the azimuthal asymmetry observed in the dust emission at 1.3 mm. We find that companions more massive than Jupiter orbiting within 70 AU from the central star might produce azimuthal asymmetries in the disk surface density between 70 AU and 90 AU, characterized by a density contrast similar to the variation in the dust intensity observed in LkH$\alpha$ 330 disk.

We argue that the disk–planet interaction might also lead to azimuthal variations in the millimeter-wave dust opacity and dust temperature, so that the resulting dust continuum emission at 1.3 mm might depend on a complex interplay between asymmetries in the dust density, opacity, and temperature. Constraining the properties of possible unseen companions from millimeter-wave observations therefore requires disentangling these three different contributions. We suggest that this can be achieved by mapping the disk emission in both optically thin and thick molecular tracers, as well as in the dust continuum emission at multiple wavelengths between 1 mm and 1 cm.

We discussed alternative explanations for the observed asymmetry in LkH$\alpha$ 330 which does not require the presence of companions: Rossby waves instabilities, baroclinic instabilities, disk warping, and disk shadowing. We argue that the first two processes might not apply to the outer regions of circumstellar disks, while the second two cannot be ruled out by existing observations.

We conclude that, although the simulations of the interaction between the circumstellar material and possible companions orbiting within about 70 AU from LkH$\alpha$ 330 provide promising similarities with CARMA data, further observations in both the dust and molecular gas emission are required to derive firm conclusions on the origins of the asymmetry observed in LkH$\alpha$ 330 disk.

We thank the OVRO/CARMA staff and the CARMA observers for their assistance in obtaining the data. Support for CARMA construction was derived from the Gordon and Betty Moore Foundation; the Kenneth T. and Eileen L. Norris Foundation; the James S. McDonnell Foundation; the Associates of the California Institute of Technology; the University of Chicago; the States of California, Illinois, and Maryland; and the National Science Foundation. Ongoing CARMA development and operations are supported by the National Science Foundation under a cooperative agreement, and by the CARMA partner universities. We acknowledge support from the Owens Valley Radio Observatory, which is supported by the National Science Foundation through grant AST-1140063. A.I. and J.M.C. acknowledge support from NSF award AST-1109334. We thank Adam Kraus for sharing unpublished results.

## APPENDIX

## FOURIER TRANSFORM OF A TWO-DIMENSIONAL GAUSSIAN FUNCTION

We report here the derivation of the Fourier transform of a 2D Gaussian function expressed in Cartesian coordinates. We start from the formulation of a 2D Gaussian function centered in the origin and oriented along the Cartesian axes,

$$g_0(x, y) = A \times \exp\left(-\frac{x^2}{2\sigma_{\rm maj}^2}\right) \times \exp\left(-\frac{y^2}{2\sigma_{\rm min}^2}\right), \quad \text{(A1)}$$

where $A$ is the amplitude, and $\sigma_{\rm maj}$ and $\sigma_{\rm min}$ are the semi-major and semi-minor axes, respectively.

We then derive the general formulation for a 2D Gaussian function by applying a rotation by the angle $\theta$ followed by a translation by $x_0$ and $y_0$. In this way, the general expression for a 2D Gaussian function assumes the form

$$g(x, y) = A \times \exp\left\{-\frac{[(x - x_0)\cos\theta + (y - y_0)\sin\theta]^2}{2\sigma_{\rm maj}^2}\right\} \times \exp\left\{-\frac{[(x - x_0)\sin\theta - (y - y_0)\cos\theta]^2}{2\sigma_{\rm min}^2}\right\}. \quad \text{(A2)}$$

The Fourier transform of Equation (A2) can be derived from the Fourier transform of Equation (A1) by applying the rotation and translation properties of the Fourier transform. The first states that an anti-clockwise rotation of a function by an angle $\theta$ implies that its Fourier transform is also rotated anti-clockwise by the same angle. The second states that a shift in position of a function by an amount $x_0$ corresponds to a phase change in its Fourier transform by $\exp(i2\pi x_0 u)$.

The Fourier transform of Equation (A1) is

$$G_0(u, v) = \int\int_{-\infty}^{+\infty} g_0(x, y)\exp[-i2\pi(ux + vy)]dxdy \quad \text{(A3)}$$

$$= A \times \int\int_{-\infty}^{+\infty} \exp\left(-\frac{x^2}{2\sigma_{\rm maj}^2}\right)\exp(-i2\pi ux)dx \times \exp\left(-\frac{y^2}{2\sigma_{\rm min}^2}\right)\exp(-i2\pi vy)dy \quad \text{(A4)}$$

$$= A \times F\left(\exp\left(-\frac{x^2}{2\sigma_{\rm maj}^2}\right)\right) \times F\left(\exp\left(-\frac{y^2}{2\sigma_{\rm min}^2}\right)\right), \quad \text{(A5)}$$

where $F(\exp(-(x^2/2\sigma_{\rm maj}^2))) = \sqrt{2\pi}\sigma_{\rm maj}\exp(-2\pi^2u^2\sigma_{\rm maj}^2)$ is the Fourier transform of a mono-dimensional Gaussian function. The Fourier transform of Equation (A1) therefore becomes

$$G_0(u, v) = A \times 2\pi\sigma_{\rm maj}\sigma_{\rm min}\exp\left[-2\pi^2\left(u^2\sigma_{\rm maj}^2 + v^2\sigma_{\rm min}^2\right)\right]. \quad \text{(A6)}$$

We first apply the rotation defined by

$$u' = u\cos\theta + v\sin\theta \quad \text{(A7)}$$

$$v' = -u\sin\theta + v\cos\theta. \quad \text{(A8)}$$

This leads to the equation

$$G(u, v) = A \times 2\pi\sigma_{\rm maj}\sigma_{\rm min}\exp\left[-2\pi^2\left((u\cos\theta + v\sin\theta)^2\sigma_{\rm maj}^2 + (-u\sin\theta + v\cos\theta)^2\sigma_{\rm min}^2\right)\right]. \quad \text{(A9)}$$

The translation is then performed by applying a phase shift corresponding to $\exp[-2\pi i(x_0u + y_0v)]$, which results in

$$G(u, v) = A \times 2\pi\sigma_{\rm maj}\sigma_{\rm min}\exp\left[-2\pi^2\left((u\cos\theta + v\sin\theta)^2\sigma_{\rm maj}^2 + (-u\sin\theta + v\cos\theta)^2\sigma_{\rm min}^2\right)\right] \times \exp[-2\pi i(x_0u + y_0v)]. \quad \text{(A10)}$$

The real and imaginary part of Equation (A10) can therefore be expressed as

$$\Re(G(u, v)) = A \times 2\pi\sigma_{\rm maj}\sigma_{\rm min} \times \exp\left[-2\pi^2\left((u\cos\theta + v\sin\theta)^2\sigma_{\rm maj}^2 + (-u\sin\theta + v\cos\theta)^2\sigma_{\rm min}^2\right)\right] \times \cos[-2\pi(x_0u + y_ov)] \quad \text{(A11)}$$

$$\Im(G(u, v)) = A \times 2\pi\sigma_{\rm maj}\sigma_{\rm min} \times \exp\left[-2\pi^2\left((u\cos\theta + v\sin\theta)^2\sigma_{\rm maj}^2 + (-u\sin\theta + v\cos\theta)^2\sigma_{\rm min}^2\right)\right] \times \sin[-2\pi(x_0u + y_ov)]. \quad \text{(A12)}$$

## REFERENCES


Andrews, S. M., Wilner, D. J., Espaillat, C., et al. 2011, ApJ, 732, 42
Andrews, S. M., Wilner, D. J., Hughes, A. M., Qi, C., & Dullemond, C. P. 2009, ApJ, 700, 1502
Armitage, P. J. 2011, ARA&A, 49, 195
Arnold, T. J., Eisner, J. A., Monnier, J. D., & Tuthill, P. 2012, ApJ, 750, 119
Birnstiel, T., Dullemond, C. P., & Pinilla, P. 2013, A&A, 550, L8
Brown, J. M., Blake, G. A., Qi, C., Dullemond, C. P., & Wilner, D. J. 2008, ApJL, 675, L109
Brown, J. M., Rosenfeld, K. A., Andrews, S. M., Wilner, D. J., & van Dishoeck, E. F. 2012, ApJL, 758, L30
Bryden, G., Chen, X., Lin, D. N. C., Nelson, R. P., & Papaloizou, J. C. B. 1999, ApJ, 514, 344
Casassus, S., van der Plas, G., M, S. P., et al. 2013, Natur, 493, 191
Chiang, E. I., & Goldreich, P. 1997, ApJ, 490, 368
Cieza, L. A., Mathews, G. S., Williams, J. P., et al. 2012a, ApJ, 752, 75
Cieza, L. A., Schreiber, M. R., Romero, G. A., et al. 2012b, ApJ, 750, 157
Cohen, M., & Kuhi, L. V. 1979, ApJS, 41, 743
Crida, A., Baruteau, C., Kley, W., & Masset, F. 2009, A&A, 502, 679
Crida, A., Morbidelli, A., & Masset, F. 2006, Icar, 181, 587
Crida, A., Morbidelli, A., & Masset, F. 2007, A&A, 461, 1173
Currie, T., & Sicilia-Aguilar, A. 2011, ApJ, 732, 24
Dawson, R. I., Murray-Clay, R. A., & Fabrycky, D. C. 2011, ApJL, 743, L17
de Val-Borro, M., Artymowicz, P., D'Angelo, G., & Peplinski, A. 2007, A&A, 471, 1043
Dodson-Robinson, S. E., & Salyk, C. 2011, ApJ, 738, 131
Dong, R., Hashimoto, J., Rafikov, R., et al. 2012, ApJ, 760, 111
Draine, B. T. 2006, ApJ, 636, 1114
Dutrey, A., Guilloteau, S., Piétu, V., et al. 2008, A&A, 490, L15
Fukagawa, M., Hayashi, M., Tamura, M., et al. 2004, ApJL, 605, L53
Grady, C. A., Muto, T., Hashimoto, J., et al. 2013, ApJ, 762, 48
Hashimoto, J., Tamura, M., Muto, T., et al. 2011, ApJL, 729, L17
Huélamo, N., Lacour, S., Tuthill, P., et al. 2011, A&A, 528, L7
Hughes, A. M., Andrews, S. M., Espaillat, C., et al. 2009, ApJ, 698, 131
Ireland, M. J., & Kraus, A. L. 2008, ApJL, 678, L59
Isella, A., Carpenter, J. M., & Sargent, A. I. 2009, ApJ, 701, 260
Isella, A., Carpenter, J. M., & Sargent, A. I. 2010a, ApJ, 714, 1746
Isella, A., Natta, A., Wilner, D., Carpenter, J. M., & Testi, L. 2010b, ApJ, 725, 1735
Isella, A., Pérez, L. M., & Carpenter, J. M. 2012, ApJ, 747, 136
Jang-Condell, H., & Turner, N. J. 2012, ApJ, 749, 153
Johnson, B. M., & Gammie, C. F. 2006, ApJ, 636, 63
Klahr, H. H., & Bodenheimer, P. 2003, ApJ, 582, 869
Kraus, A. L., & Ireland, M. J. 2012, ApJ, 745, 5
Larwood, J. D., & Kalas, P. G. 2001, MNRAS, 323, 402
Lesur, G., & Papaloizou, J. C. B. 2010, A&A, 513, A60
Lin, D. N. C., & Papaloizou, J. 1979, MNRAS, 188, 191
Lin, D. N. C., & Papaloizou, J. 1986, ApJ, 307, 395
Lyra, W., & Mac Low, M.-M. 2012, ApJ, 756, 62
Masset, F. 2000, A&AS, 141, 165
Masset, F. S. 2001, ApJ, 558, 453
Masset, F. S. 2002, A&A, 387, 605
Masset, F. S., & Casoli, J. 2009, ApJ, 703, 857
Masset, F. S., & Casoli, J. 2010, ApJ, 723, 1393
Masset, F. S., Morbidelli, A., Crida, A., & Ferreira, J. 2006, ApJ, 642, 478

Masset, F. S., & Ogilvie, G. I. 2004, ApJ, 615, 1000
Masset, F. S., & Papaloizou, J. C. B. 2003, ApJ, 588, 494
Mayama, S., Hashimoto, J., Muto, T., et al. 2012, ApJL, 760, L26
Morales-Calderón, M., Stauffer, J. R., Stassun, K. G., et al. 2012, ApJ, 753, 149
Muto, T., Grady, C. A., Hashimoto, J., et al. 2012, ApJL, 748, L22
Muzerolle, J., Allen, L. E., Megeath, S. T., Hernández, J., & Gutermuth, R. A. 2010, ApJ, 708, 1107
Ohashi, N. 2008, Ap&SS, 313, 101
Osterloh, M., & Beckwith, S. V. W. 1995, ApJ, 439, 288
Pérez, L., Lamb, J., Woody, D., Carpenter, J. M., & Zauderer, A. 2010, ApJ, 724, 493
Pérez, L. M., Carpenter, J. M., Chandler, C. J., et al. 2012, ApJL, 760, L17
Petersen, M. R., Julien, K., & Stewart, G. R. 2007a, ApJ, 658, 1236
Petersen, M. R., Stewart, G. R., & Julien, K. 2007b, ApJ, 658, 1252
Piétu, V., Dutrey, A., Guilloteau, S., Chapillon, E., & Pety, J. 2006, A&A, 460, L43
Piétu, V., Guilloteau, S., & Dutrey, A. 2005, A&A, 443, 945
Pinilla, P., Birnstiel, T., Ricci, L., et al. 2012, A&A, 538, A114
Pollack, J. B., Hollenbach, D., Beckwith, S., et al. 1994, ApJ, 421, 615
Raettig, N., Lyra, W., & Klahr, H. 2013, ApJ, 765, 115
Rafikov, R. R. 2002, ApJ, 572, 566
Regály, Z., Juhász, A., Sándor, Z., & Dullemond, C. P. 2012, MNRAS, 419, 1701
Ricci, L., Testi, L., Natta, A., & Brooks, K. J. 2010, A&A, 521, A66
Rosenfeld, K. A., Qi, C., Andrews, S. M., et al. 2012, ApJ, 757, 129
Sault, R. J., Teuben, P. J., & Wright, M. C. H. 1995, in ASP Conf. Ser., 77, Astronomical Data Analysis Software and Systems IV, ed. R. A. Shaw, H. E. Payne, & J. J. E. Hayes (San Franciso, CA: ASP), 433
Strom, K. M., Strom, S. E., Edwards, S., Cabrit, S., & Skrutskie, M. F. 1989, AJ, 97, 1451
Tang, Y.-W., Guilloteau, S., Piétu, V., et al. 2012, A&A, 547, A84
Thalmann, C., Grady, C. A., Goto, M., et al. 2010, ApJL, 718, L87
van der Marel, N., van Dishoeck, E. F., Bruderer, S., et al. 2013, Sci, 340, 1199
Wahhaj, Z., Liu, M. C., Nielsen, E. L., et al. 2013, ApJ, 773, 179
Wolf, S., & Klahr, H. 2002, ApJL, 578, L79
Zacharias, N., Finch, C. T., Girard, T. M., et al. 2013, AJ, 145, 44
Zhu, Z., Nelson, R. P., Dong, R., Espaillat, C., & Hartmann, L. 2012, ApJ, 755, 6
Zhu, Z., Nelson, R. P., Hartmann, L., Espaillat, C., & Calvet, N. 2011, ApJ, 729, 47